Thermal analysis of magnetic shields for induction heating

Peter Sergeant[1,2], Dietrich Hectors[3], Luc Dupré[1], and Koen Van Reusel[1,3]

[1]Dept. Electrical Energy, Systems & Automation, Ghent University, St-Pietersnieuwstraat 41, 9000 Ghent, Belgium
[2]Dept. Electrotechnology, Faculty of Applied Engineering Sciences, University College Ghent, Ghent, Belgium
[3]Dept. Electrical Engineering, KU Leuven, Kasteelpark Arenberg 10, 3001 Heverlee, Belgium

***Abstract*—For the design of magnetic shields for induction heating, it is useful to analyze not only the magnetic field reduction, but also the temperature behaviour of the shield. The latter is heated by its electromagnetic losses and by thermal radiation from the workpiece. A coupled thermal-electromagnetic axisymmetric finite element model is used to study the temperature of a shield for an axisymmetric induction heater, highlighting the effect of the radius, height, thickness and material of the shield on its temperature and magnetic shielding factor. Also the effect of the frequency and the workpiece dimensions is investigated. The model is validated by measuring the magnetic induction, the induced currents in the shield and the temperature of the shield on the experimental setup. The temperature is unacceptably high for shields close to the excitation coil, especially if the shield height is lower than the workpiece height. Although the study is carried out for one specific induction heater geometry, the paper indicates the effect on the shield temperature of parameters such as geometry, material and frequency so that the results are useful also for other induction heating configurations.**

***Index Terms*—Shielding, Finite element analysis, Optimization**

I. Introduction

In magnetic shield design problems, the optimization goals are usually the minimization of the field in a predefined area – the target region – and the minimization of the electromagnetic losses in the shield [1], [2]. However, it is also useful to include thermal aspects: a shield may obtain a high temperature due to electromagnetic losses and heat radiation from the workpiece.

In section II, the steady-state temperature of the workpiece is simulated and experimentally validated for the unshielded case by a coupled thermal-electromagnetic finite element model (FEM). In section III, a simplified thermal-electromagnetic FEM calculates the temperature of the shield as a function of the radial position and height of the shield. In section IV, the temperature and shielding performance are studied for several shield thicknesses, material properties (conductivity, permeability), frequencies, and workpiece geometries. In section V, the shield is optimized to obtain a given shielding efficiency without exceeding a limit temperature.

II. Coupled thermal-electromagnetic FEM to study the workpiece temperature

A coupled axisymmetric thermal and electromagnetic FEM finds as a function of time the temperature distribution in the workpiece. Fig. 1 shows the axisymmetric geometry of the induction heater with properties in Table I. The copper shield shown in Fig. 1a and c is however not present for the determination of the workpiece temperature. The thermal time-stepping model solves the equation for the temperature T:

$$\rho c_{\mathrm{p}} \frac{\partial T}{\partial t} - \nabla \cdot (\lambda \nabla T) = Q_{\mathrm{em}} \quad (1)$$

$$\mathbf{n} \cdot (\lambda_1 \nabla T_1 - \lambda_2 \nabla T_2) = -Q_{\mathrm{conv}} - Q_{\mathrm{rad}} \quad (2)$$

with ρ the mass density, c_{p} the heat capacity, and λ the thermal conductivity. Eq. 2 is the boundary condition on a boundary between media 1 and 2 with $\mathbf{n}$ the normal vector. The workpiece is heated by resistive electromagnetic heating Q_{em}, which is a volume power density (in W/m^3). It is cooled by convection Q_{conv} and radiation Q_{rad}, which are heat flux densities (in W/m^2) imposed on the workpiece surface.

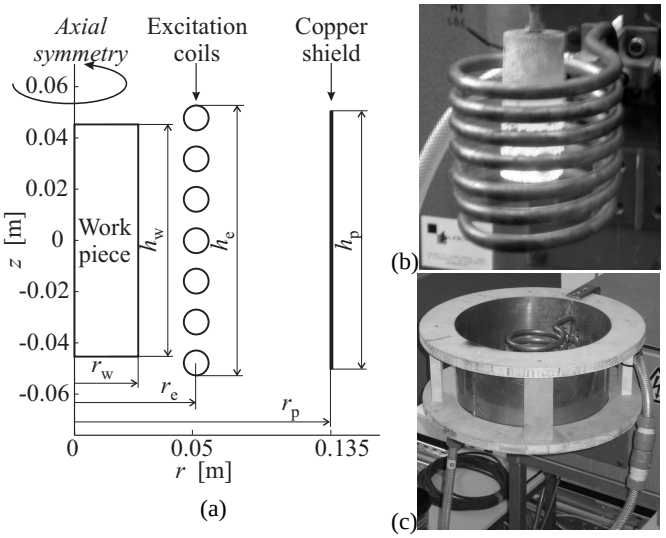

Fig. 1. (a) Geometry of the shielded axisymmetric induction heating device with dimensions in Table I; (b) unshielded induction heater with workpiece and (c) induction heater with shield in a wooden frame. The shield is a 1 mm thick copper plate with r_{p} = 0.135 m and h_{p} = 0.15 m

The convection is $Q_{\mathrm{conv}} = h(T - T_0)$ with h = 10 W/(m^{2}K) calculated from [3] and T_0 = 20°C the ambient temperature.

The total radiated power P_{rad} of the workpiece in stainless steel is $P_{\mathrm{rad}} = \int_{A_{\mathrm{w}}} Q_{\mathrm{rad}}\, \mathrm{d}a = \epsilon_{\mathrm{w}} c_\sigma \int_{A_{\mathrm{w}}} (T^4 - T_0^4)\, \mathrm{d}a$ [4] with c_σ the Stefan-Boltzmann constant (5.670×10^{-8} W/m^2/K^4) and A_{w} the workpiece surface. The emissivity ϵ_{w} of the workpiece was measured and was observed to vary between 0.5 and 0.97 depending on the oxidation state. For the simulation of the workpiece temperature, the value 0.97 was chosen because the workpiece was completely oxidized. The thermal conductivity

Manuscript received May 3th 2008. Corresponding author: P. Sergeant (e-mail: Peter.Sergeant@UGent.be). This work was supported by the FWO project G.0082.06, by the GOA project BOF 07/GOA/006 and the IAP project P6/21. The first author is a postdoctoral fellow with the FWO.

$\lambda_{\rm w}$, the mass density $\rho_{\rm w}$, and the heat capacity $c_{\rm p,w}$ of the workpiece are temperature dependent expressions found from [5], causing the numerical model to be nonlinear. Typical values of these quantities are given in Table I.

To determine the total electromagnetic power $P_{\rm em}$, at every time step, a time-harmonic and quasi-static electromagnetic FEM is solved with the vector potential as unknown: $-\frac{1}{\mu_0}\nabla^2\mathbf{A} + \mathrm{j}\omega\sigma_{\rm w}\mathbf{A} = \mathbf{J}_{\rm e}$. Then, $P_{\rm em} = \int_{V_{\rm w}} Q_{\rm em}\ \mathrm{d}v = \int_{V_{\rm w}} \sigma\omega^2|\mathbf{A}|^2\ \mathrm{d}v$ with $V_{\rm w}$ the volume of the workpiece. The electrical conductivity σ is temperature dependent (Table I).

To validate the model, the time evolution of the temperature is simulated and measured by a sensor Thermovision A40, starting from a cold workpiece in stainless steel. The excitation current in the 7-turn induction heater was set to 532 A rms at 26.8 kHz. The steady state temperature of the workpiece of 50 mm diameter and 90 mm height is 1170°C (simulated) and 1212°C (measured) with a time constant of 168 s (simulated) and 201 s (measured) as shown in Fig. 2.

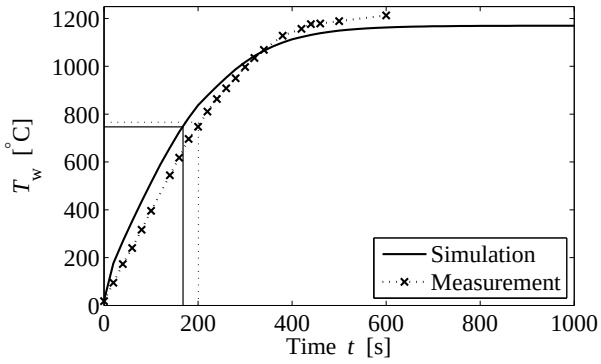

Fig. 2. Workpiece temperature has steady-state of 1170°C (simulated) or 1212°C (measured); time constant is 168 s (simulated) or 201 s (measured)

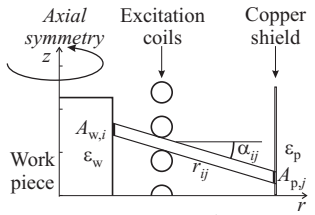

Fig. 3. Radiation from workpiece section $A_{{\rm w},i}$ to shield section $A_{{\rm p},j}$

III. Simplified thermal-electromagnetic FEM to study shield temperature

Secondly, the temperature of the 1 mm thick copper shield is studied. To reduce the CPU time of the simulation, the coupling between the electromagnetic and the temperature model is broken. The heat problem (1) and (2) is solved by a transient FEM in the shield only, with the following source terms.

The negative source terms that cool down the shield are applied at all its boundaries: free natural convection in air $Q_{\rm conv,p} = h(T - T_0)$ and heat radiation to infinity $Q_{\rm rad,p} = \epsilon_{\rm p} c_\sigma (T^4 - T_0^4)$ wherein $\epsilon_{\rm p}$ is the emissivity of the shield.

The positive source terms that heat the shield are the electromagnetic losses $Q_{\rm em}$ and the heat radiation $Q_{\rm rad}$ from the workpiece to the shield. $Q_{\rm em}$ in the shield is found from a linear time-harmonic electromagnetic model with (full) geometry of Fig. 1a. The broken coupling between the thermal and the electromagnetic FEM means that the latter assumes temperature independent material properties, chosen based on a workpiece temperature equal to the steady-state value found in section II (1170°C). $P_{\rm rad}$ is the total power radiated from the workpiece to the shield through the air gaps between the excitation coil windings. In the thermal FEM of the shield only, $P_{\rm rad}$ is a heat flux boundary condition on the shield edge that is illuminated by the workpiece as shown in Fig. 3.

$$P_{\rm rad} = \epsilon_{\rm w}\epsilon_{\rm p} c_\sigma \sum_{i=1}^{6}\sum_{j=1}^{N} F_{{\rm wp},ij}\ A_{{\rm w},i}\ (T_i^4 - T_j^4) \quad (3)$$

$$F_{{\rm wp},ij} = \frac{\cos^2\alpha_{ij}}{\pi r_{ij}^2} A_{{\rm p},j} \quad (4)$$

The shield is divided in a sufficiently large number N of segments with total surface $A_{\rm p}$. The surface $A_{{\rm p},j}$ is illuminated by surfaces $A_{{\rm w},i}$, $i = 1 \ldots 6$ (the number of gaps between the 7 excitation coils). The height of the surfaces $A_{{\rm w},i}$ is determined by the space between the adjacent excitation coils and the angle α_{ij}.

The experimental validation of this model is carried out in three ways, for the same excitation current as in section II (532 A at 26.8 kHz) and for a shield with radial position $r_{\rm p}$ = 0.135 m and height $h_{\rm p}$ = 0.150 m.

Firstly, the steady-state temperature of the shield is measured and simulated. Both agreed well: 83.1°C and 87.7°C respectively. Regarding the shield, it was observed that the emissivity of the used copper samples strongly depends on the temperature: during the experiment, the emissivity of the copper was identified in real-time by measuring the temperature both by a thermocouple and by the Thermovision sensor that uses

TABLE I
Geometrical and electromagnetic properties

Excitation	Radius	$r_{\rm e}$	47.4 mm
	Total height	$w_{\rm e}$	104.8 mm
	Number of turns	$t_{\rm e}$	7
	Conductor radius	$h_{\rm e}$	4.8 mm
	Current	$I_{\rm e}$	532 A rms
	Frequency	f	26.8 kHz
Workpiece	Outer radius	$r_{\rm w}$	25.0 mm
	Height	$h_{\rm w}$	90.0 mm
	Magnetic permeability	$\mu_{\rm w}$	μ_0
	Mass density$^{(*)}$	$\rho_{\rm w}$	7350 kg/m^3
	Electrical conductivity$^{(*)}$	$\sigma_{\rm w}$	0.799 MS/m
	Thermal conductivity$^{(*)}$	$\lambda_{\rm w}$	30.3 W/(m.K)
	Heat capacity$^{(*)}$	$c_{\rm p,w}$	667 J/(kg.K)
	Emissivity$^{(*)}$	$\epsilon_{\rm w}$	0.5–0.97
Shield	Inner radius	$r_{\rm p}$	(60–250 mm)
	Height	$h_{\rm p}$	(0–400 mm)
	Sheet thickness	$t_{\rm p}$	1.00 mm
	Electrical conductivity	$\sigma_{\rm p}$	50 MS/m
	Magnetic permeability	$\mu_{\rm p}$	μ_0
	Thermal conductivity$^{(**)}$	$\lambda_{\rm p}$	400 W/(m.K)
	Mass density$^{(**)}$	$\rho_{\rm p}$	8900 kg/m^3
	Heat capacity$^{(**)}$	$c_{\rm p,p}$	385 J/(kg.K)
	Emissivity$^{(**)}$	$\epsilon_{\rm p}$	0.15
Target area	Inner radius	$r_{\rm ta}$	0.30 m
	Width	$w_{\rm ta}$	1.0 m
	Cross section height	$h_{\rm ta}$	1.0 m

$^{(*)}$ At steady-state temperature of 1170°C. $^{(**)}$ At 80°C.

the emissivity to determine the temperature. The emissivity at 83.1°C shield temperature turned out to be 0.15. This value was used in the simulations.

Secondly, the induced currents in the shield were simulated and measured by a Rogowski current probe, for five values of the excitation current. For all five measurements, the measured induced current was about 11% higher than the simulated one, e.g. for 219.2 A excitation current, the measured and simulated shield currents were 186.7 A and 167.4 A respectively.

The third way of validation is the comparison of the magnetic flux density that is simulated and measured (by a field meter *Maschek ESM-100*) in the target region. In Fig. 4, it can be seen that in absence of shields, the measured and simulated curves are almost coinciding. With the shield present, the deviation increases with increasing radial distance, probably because the lower field levels are influenced by the magnetic field of the generator. Fourier analysis was carried out to avoid disturbing fields that have other frequencies. As a reference, field curves are shown for a small shield short to the excitation coils and for a large shield at large distance.

The electromagnetic and radiated power $P_{\rm em}$ and $P_{\rm rad}$ in the shield depend on the position $r_{\rm p}$ and height $h_{\rm p}$ of the shield as shown in Fig. 5a and b. $P_{\rm em}$ decreases slightly with increasing $h_{\rm p}$, and decreases strongly with increasing $r_{\rm p}$. $P_{\rm rad}$ is usually much higher than $P_{\rm em}$ at the considered workpiece temperature: it increases more or less linearly with $h_{\rm p}$ if $h_{\rm p}$ is lower than the inductor height (≈0.1 m), and "saturates" for higher $h_{\rm p}$ to a constant value of approximately 300 W.

The average flux density $B_{\rm avg}$ in the target region with dimensions in Table I is very low for high shields short to the induction heater (Fig. 5c). When increasing $r_{\rm p}$, the height $h_{\rm p}$ should increase more or less proportionally to achieve the same shielding performance. The field reduction of three shield configurations can be seen as a function of the radius in Fig. 4.

The temperature distribution in the shield is almost uniform because it is thin and a good thermal conductor. Therefore, the shield temperature can be studied by using the average shield temperature instead of the entire temperature distribution in the shield. Fig. 5d shows the average steady-state temperature in the shield. It can be observed that the temperature decreases with increasing $r_{\rm p}$, because $P_{\rm em}$ and $P_{\rm rad}$ decrease. With increasing $h_{\rm p}$, the temperature of the shield decreases although $P_{\rm em} + P_{\rm rad}$ increases. The reason is that the larger surface of the shield causes better cooling by convection and radiation.

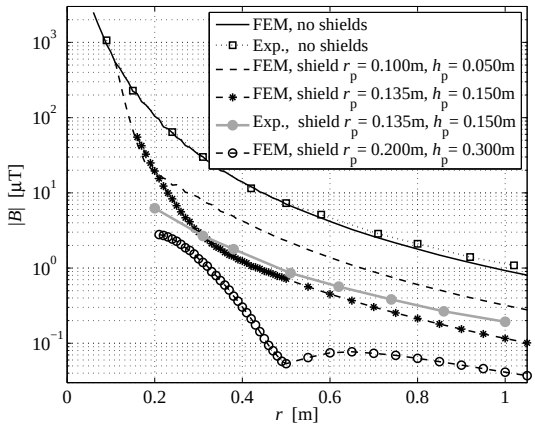

Fig. 4. Measured and simulated induction in the target region for the unshielded and shielded induction heater for 180.7 A excitation current.

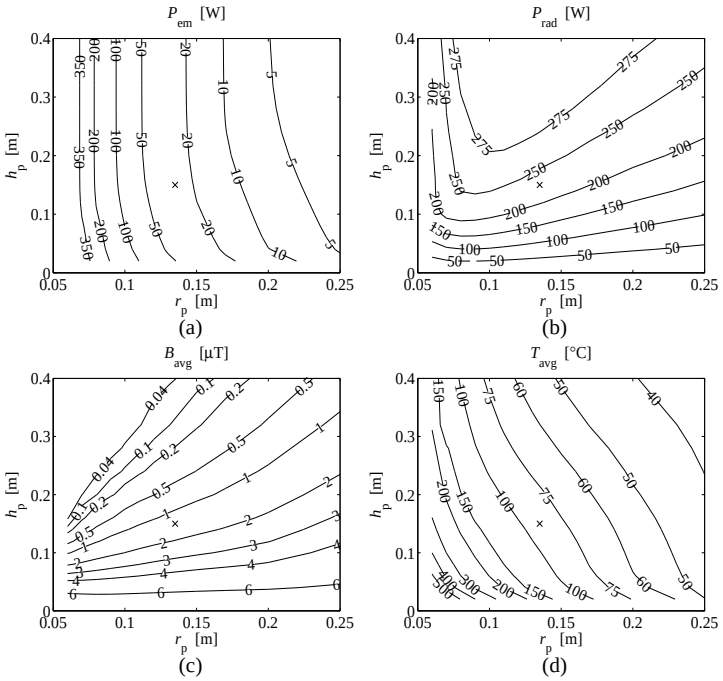

Fig. 5. As a function of the radial position $r_{\rm p}$ and the height $h_{\rm p}$ of the 1 mm thick passive shield, (a) electromagnetic power $P_{\rm em}$, (b) radiated power $P_{\rm rad}$ (c) average magnetic induction in the target region and (d) average temperature in °C. The excitation current is 532 A. The experimental shield is indicated by a cross.

IV. Influence on Shielding Performance and Shield Temperature of Shield Material, Workpiece Geometry, Shield Thickness and Frequency

Other material for the shield – with different electrical conductivity and magnetic permeability than copper – affects the electromagnetic power, but also the radiated power because of a change in emissivity. Only taking into account the change in electromagnetic power, Fig. 6 shows the steady state temperature of the "experimental" shield with $r_{\rm p}$ = 0.135 m and $h_{\rm p}$ = 0.150 m for several conductivities and permeabilities. Copper with σ = 50 MS/m and $\mu_{\rm r}$ = 1 results almost in the lowest possible temperature: 87.7°C. If the copper material is replaced by a ferromagnetic electrical steel with σ= 5.9 MS/m and $\mu_{\rm r}$ = 372, the temperature increases from 87.7 to 238.8°C. The maximum in the curve can be explained as follows. For high σ, a further increase of σ reduces $P_{\rm em}$ because the induced currents see less resistance. For low σ, an increase of σ increases $P_{\rm em}$ because the induced current I is more or less proportional to σ, and $P_{\rm em} \sim I^2$.

Concerning the **workpiece geometry**, Fig. 7a shows that the average temperature in the shield increases with increasing outer radius $r_{\rm w}$ and height $h_{\rm w}$ of the workpiece. The reason is that the radiated power – shown in Fig. 7c – increases because it is proportional to the workpiece surface: $P_{\rm rad} \sim A_{\rm w} \sim r_{\rm w} h_{\rm w}$. The electromagnetic power however – see Fig. 7b – decreases as more eddy currents in the workpiece reduce the stray field of the induction heater, i.e. the field that is not

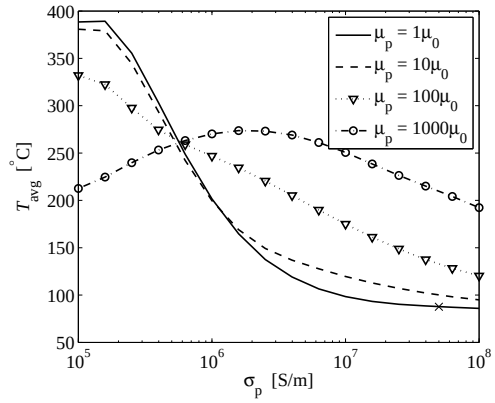

Fig. 6. Average temperature in °C in the 1 mm thick copper shield (r_p = 0.135 m and h_p = 0.15 m) as a function of the electrical conductivity σ_p and the magnetic permeability μ_p. The position of the copper shield is indicated by a cross. The radiation P_rad is assumed to be constant (constant workpiece temperature and emissivity of the shield)

coupled to the workpiece. Here, we assumed that the shield does not influence the excitation current amplitude and the workpiece temperature. Nevertheless, the decrease of P_em has almost no influence on T_avg as $P_\mathrm{em} \ll P_\mathrm{rad}$ at the steady-state temperature found in section II.

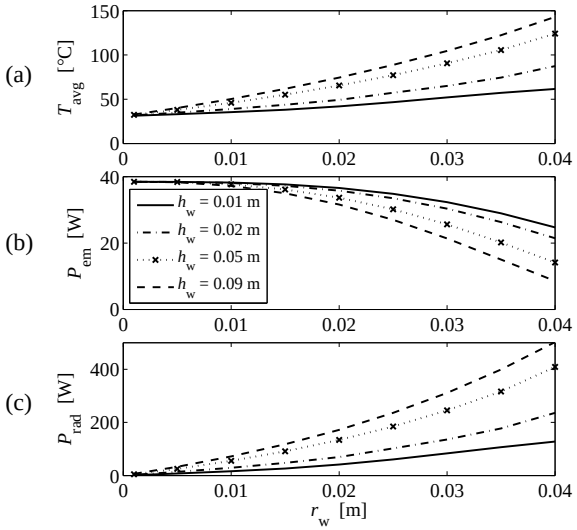

Fig. 7. (a) Average temperature, (b) electromagnetic power P_em and (c) radiated power P_rad in the shield as a function of the geometry of the workpiece: outer radius r_w and height h_w.

If the **shield thickness** t_p is changed, few influence is observed on the temperature. P_rad is independent of t_p. For shields thicker than the penetration depth δ (0.44 mm in copper at 26.8 kHz), the field reduction and P_em are almost independent of the thickness. For shields with $t_\mathrm{p} \ll \delta$, the field reduction is less efficient.

If the **frequency** is higher than 5 kHz – the frequency where δ equals the shield thickness of 1 mm – P_em increases with the square root of the frequency: the induced currents flow in a thinner region resulting in an increased AC resistance. For lower frequency, P_em is quadratic with the frequency, but in amplitude negligible compared to P_rad. P_rad shows almost no change in the hypothetic case that the workpiece temperature remains 1170°C. However, increasing the frequency also increases the power in the workpiece, its temperature and the power radiated to the shield. The average field in the target area decreases with increasing frequency up to 5 kHz; for higher frequency, B_avg remains approximately constant.

V. Optimization of the shield for good shielding efficiency without exceeding temperature limit

An optimization is carried out to find a shield geometry that reduces the average magnetic field norm in the target region to maximally 1 μT without exceeding a shield temperature of 100°C. The parameters to optimize are the shield position r_p (in the range 0.06 – 0.25 m) and the shield height h_p (in the range 0 – 0.40 m). This is a multi-objective optimization problem. The first objective aims at achieving sufficient field reduction. This means that the rectangular search domain in Fig. 5c is restricted to the area above the line B = 1 μT. The second goal about the temperature means that in Fig. 5d, the search domain is restricted to the region right of the contour line 100°C. It can be seen that the experimentally built shield (indicated by a cross) is approximately the best solution. Of course, an optimization routine should find the solution without scanning the whole domain. We used the Matlab routine *fgoalattain* to solve this problem. The optimization routine used 32 function evaluations and returned the optimal solution which is close to the experimental shield: r_p = 0.1208 m and h_p = 0.1578 m, resulting in B_avg = 1.0 μT and T_avg = 100°C.

VI. Conclusion

When shielding the magnetic stray field of an induction heating device, the shield temperature increases as a result of electromagnetic resistive heating and radiation of heat from the workpiece. The electromagnetic power – caused by induced currents in the copper shield – is rather small in a copper shield, but very large in a steel shield at the considered frequency of 26.8 kHz. It decreases weakly with the height of the shield and strongly with the radial distance between the shield and the workpiece. The radiated heat is usually dominant in the considered induction heater. It increases strongly with the height of the shield until the shield height is the same as the height of the workpiece and becomes more or less constant for higher heights. The radiated power decreases weakly with increasing radius of the shield. An optimization shows that a good field reduction and low shield temperature can be achieved if the shield is rather high but at a large radial distance from the workpiece.

References

[1] P. Sergeant, L. Dupré, M. De Wulf and J. Melkebeek, "Optimizing active and passive magnetic shields in induction heating by a Genetic Algorithm", *IEEE Trans. Magn.*, Vol. 39, No. 6, pp. 3486-3496, 2003.

[2] P. Sergeant, L. Dupré, and J. Melkebeek, "Space mapping method for the design of passive shields," *Journal of Applied Physics*, Vol. 99, No. 8, 08H901, Apr. 2006.

[3] S. Kakac, R.S. Shah, and W. Aung, *Handbook of Single-Phase Convective Heat Transfer*, Wiley, New York, 1987.

[4] R. Siegel and J.R. Howell, *Thermal Radiation Heat Transfer*, 4th edition, Taylor & Francis Inc., New York, 2002.

[5] K. C. Mills, Y. Su, Z. Li and R. F. Brooks, "Equations for the calculation of the thermo-physical properties of stainless steel," *ISIJ International*, Vol. 44, No. 10, pp. 1661-1668, 2004.